International Journal of Nanomedicine

Dovepress
Taylor & Francis Group

Open Access Full Text Article

ORIGINAL RESEARCH

Targeted Sustained-Release Therapy for Vulnerable Atherosclerotic Plaques Using Luteolin-Loaded Nanoparticles

Shaoshen Wang[1–3,*], Xiangxiang Shi[1,*], Xiaoqi Li[2,*], Yang Liu[1], Chaofan Wang[3], Yetong Wu[2], Yiwen Wang[3], Wei Qian[3], Xiaxia Li[2], Jing Huang[2], Dongye Li[1,3], Tongda Xu[1,3]

[1]Institute of Cardiovascular Disease Research, Xuzhou Medical University, Xuzhou, 221002, People's Republic of China; [2]Department of Cardiology, The Second Affiliated Hospital of Chongqing Medical University, Chongqing, 400010, People's Republic of China; [3]Department of Cardiology, Affiliated Hospital of Xuzhou Medical University, Xuzhou, 221006, People's Republic of China

*These authors contributed equally to this work

Correspondence: Dongye Li; Tongda Xu, Email dongyeli@xzhmu.edu.cn; 770020210441@xzhmu.edu.cn

Purpose: The early, precise, and safe management of vulnerable atherosclerotic plaques (VAPs) remains a formidable clinical challenge. Here, we present a targeted nanotherapeutic approach in which osteopontin-targeted nanoparticles encapsulate luteolin (NPs-Lut) for the precise delivery and treatment of VAPs. This engineered system enables site-specific accumulation and sustained release of luteolin at plaque sites.

Methods: We innovatively constructed an osteopontin-targeted drug delivery system designed for vulnerable atherosclerotic plaques, in which luteolin and atorvastatin were successfully encapsulated. The system demonstrated sustained-release capability in vitro, and its biosafety and histocompatibility were comprehensively evaluated both in vitro and in vivo. Moreover, therapeutic efficacy was further assessed in ApoE$^{-/-}$ mice, confirming its potential for treating atherosclerotic lesions.

Results: In vivo evaluation in ApoE$^{-/-}$ mice demonstrated that NPs-Lut markedly outperformed atorvastatin-loaded nanoparticles (NPs-AST) in attenuating plaque-associated inflammation, alleviating endoplasmic reticulum stress and foam cell apoptosis, and enhancing plaque stability. Histological analysis revealed a significant reduction in plaque and necrotic core area, accompanied by increased fibrous cap thickness and collagen deposition. By improving the aqueous solubility and bioavailability of luteolin, NPs-Lut achieved potent therapeutic efficacy at low doses while minimizing systemic toxicity.

Conclusion: This work provides a robust and translationally promising nanoplatform for the precision treatment of VAPs, offering a novel strategy for safe and effective intervention in atherosclerotic cardiovascular disease.

Keywords: luteolin, atorvastatin, noninvasive targeted therapy, delivery, vulnerable atherosclerotic plaques

Introduction

Cardiovascular diseases (CVDs)[1] remain the leading cause of mortality worldwide,[2] representing a critical global health challenge that demands urgent attention.[3] Beyond the significant reduction in patient quality of life, CVDs impose a substantial socioeconomic burden.[4] The clinical manifestations of these diseases such as myocardial infarction and ischemic stroke are primarily driven by the rupture of vulnerable atherosclerotic plaques(VAPs).[5–7] These plaques are characterized by complex pathological features, including thin fibrous caps, large lipid cores, and a multifactorial pathogenesis involving inflammation, oxidative stress, and apoptosis.[8–10] The inherent heterogeneity and complexity of VAPs have become a major barrier to precise clinical diagnosis and effective therapeutic intervention.

Current first-line treatments for atherosclerotic cardiovascular disease primarily rely on lipid-lowering agents, including statins and proprotein convertase subtilisin/kexin type 9 inhibitors (PCSK9i).[11,12] Although these therapies significantly reduce low-density lipoprotein cholesterol (LDL-C) levels and partially stabilize plaques, their overall

Received: 11 September 2025
Accepted: 17 December 2025
Published: 28 December 2025

Graphical Abstract

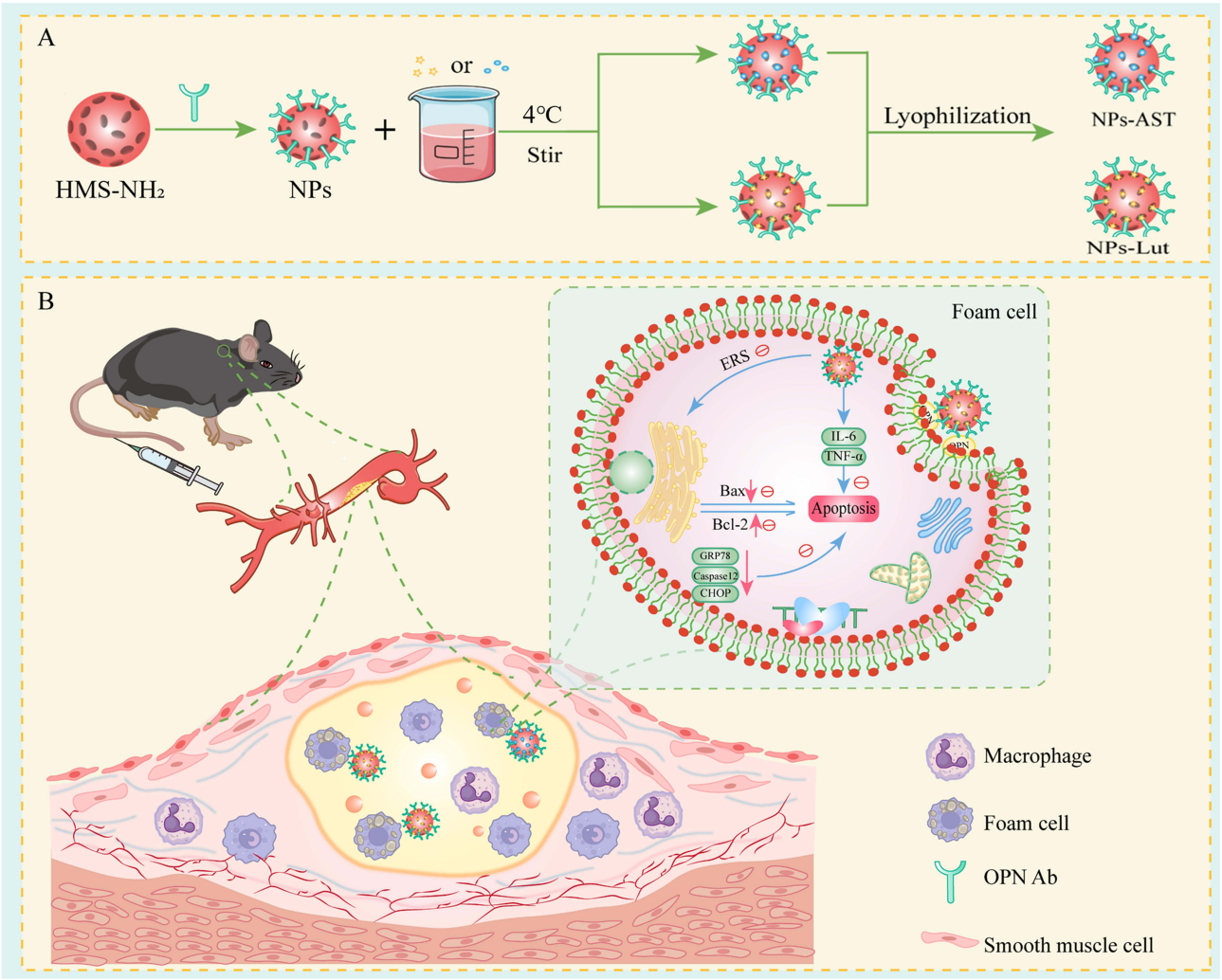

clinical efficacy remains suboptimal,[13] particularly with regard to PCSK9 inhibitors' effects on enhancing plaque stability and promoting plaque regression.[12] Furthermore, statin-associated adverse effects, such as hepatotoxicity, nephrotoxicity and rhabdomyolysis, necessitate regular monitoring of liver and renal function, limiting their long-term clinical utility and patient compliance.[14]

Inflammatory cascades and endoplasmic reticulum stress (ERS)[15,16] are key drivers in the pathogenesis of VAPs.[17–19] Luteolin (3′,4′,5,7-tetrahydroxyflavone), a natural flavonoid abundantly found in vegetables (eg, carrots, cabbages), fruits (eg, apples), and medicinal plants (eg, green tea, celery), has demonstrated potent anti-inflammatory, anti-apoptotic, and anti-atherosclerotic effects.[20–23] However, its clinical application is severely limited by extremely low water solubility[24–27] and poor bioavailability,[28–32] loading luteolin into nano-drug delivery systems (NDDS) represents a promising strategy to surmount these limitations.[33]

Our team previously developed an OPN Ab Ce6/PFP-Au NPs@SiO_2 nanoplatform capable of noninvasive, targeted imaging of VAPs. This platform demonstrates excellent biosafety, scalability, and translational potential, laying the foundation for further therapeutic innovations.[34]

Building upon these findings, this study developed a targeted luteolin-loading nanoparticles (NPs-Lut) designed to achieve precise delivery of luteolin to VAPs, leveraging the carrier properties of nanoparticles (NPs). For comparison,

a parallel formulation encapsulating the first-line lipid-lowering drug atorvastatin (NPs-AST) was constructed to systematically assess drug-loading capacity, sustained-release behavior, and biosafety.

In vitro analyses demonstrated that both NPs-Lut and NPs-AST exhibited high drug-loading efficiency, sustained-release profiles, and cytotoxicity within a safe range. In vivo studies further revealed that, compared to non-targeted controls, NPs-Lut exerted superior anti-inflammatory effects in a vulnerable plaque model—markedly reducing pro-inflammatory cytokines (IL-1β, IL-6, TNF-α), decreasing total plaque area to ~80% of the non-targeted group, shrinking necrotic core areas to ~40%, and increasing collagen content to ~130%. Notably, fibrous cap thickness was significantly enhanced in the NPs-Lut group, collectively indicating improved VAPs stability.

Both NPs-AST and NPs-Lut exhibit good lipid-lowering effects, and their effects are comparable. However, NPs-Lut demonstrated clear advantages in modulating the ERS pathway—evidenced by downregulation of GRP78, Caspase-12 and CHOP expression—and in suppressing foam cell apoptosis. These findings suggest that targeted suppression of ERS and apoptosis may represent a robust mechanism by which luteolin stabilizes VAPs.

This study is the first to report the targeted therapeutic efficacy of NPs-Lut in VAPs and to elucidate its potential molecular mechanisms. The platform demonstrates excellent targeting efficiency and favorable biosafety, with no significant abnormalities observed in liver and kidney function parameters. These findings provide critical experimental evidence supporting the clinical translation of precision nanotherapeutics for VAPs management.

Materials and Methods

Materials and Instruments

Luteolin (purity: 99.51%) and atorvastatin (purity: 99.67%) were purchased from MedChemExpress (MCE, China). Tetrachloroauric (III) acid ($HAuCl_4 \cdot 3H_2O$), Calcein-AM and propidium iodide (PI), annexin V-FITC/PI cell apoptosis kit (KGAF001); ammonia solution,3-aminopropyltrimethoxysilane (APTMS), Oil Red O, Cell Counting Kit-8 (CCK-8), absolute ethanol, phosphate-buffered saline (PBS), ELISA kits for TNF-α, IL-1β, and IL-6, and dimethyl sulfoxide (DMSO) were obtained from Sigma-Aldrich (St. Louis, MO, USA). Dulbecco's Modified Eagle Medium (DMEM) and fetal bovine serum (FBS) were purchased from Gibco (Grand Island, NY, USA), Rabbit osteopontin antibody (OPN Ab) were purchased from Abcam (Cambridge, UK). All chemicals and reagents were used as received without further purification. Zeta potential and hydrodynamic diameter measurements of nanoparticles were carried out using a Zetasizer Nano ZS90 (Malvern Instruments, UK). Quantitative real-time PCR was conducted using the ABI 7500 Real-Time PCR System (Applied Biosystems, USA). Tissue homogenization was performed with a Pro200 Precision Tissue Homogenizer (ProScientific Inc., USA).

Drug Loading and Encapsulation Efficiency of NPs-Lut and NPs-AST

Luteolin solutions were diluted with deionized water to concentrations of 0.0625 mg/mL, 0.125 mg/mL, 0.250 mg/mL, 0.500 mg/mL, and 1.000 mg/mL. Spectral scans of any luteolin solution using a UV spectrophotometer revealed a maximum absorbance at 286 nm. Absorbance values of these solutions were measured at 286 nm to plot the standard curve of luteolin in aqueous solution. 20 mg of nanoparticles were dispersed in 9 mL of deionized water and sonicated for 90 min. Subsequently, 1 mL of 1.5 mg/mL luteolin solution was added, followed by additional sonication to ensure thorough mixing. The mixture was then stirred at low speed for 20 h in the dark. Afterward, the solution was transferred to centrifuge tubes and centrifuged at 13,000 rpm. The solid precipitate was freeze-dried for 24 h to obtain drug-loaded nanoparticles. The supernatant was diluted, and its absorbance at 286 nm was measured using a UV spectrophotometer. The residual drug concentration was calculated from the standard curve to determine the drug loading and encapsulation efficiency of the nanoparticles.

$$\text{Drug Loading}(\%) = \frac{m_b - m_a}{m_{dl}} \times 100\% \tag{1}$$

$$\text{Encapsulation Efficiency}(\%) = \frac{m_b - m_a}{m_b} \times 100\% \tag{2}$$

 https://doi.org/10.2147/IJN.S566896

In the formula, ma is the mass of the drug in the supernatant (mg), mb is the total mass of the drug added to the system (mg), and mdl is the mass of the drug-loaded nanoparticles (mg). The same procedure was used to determine the standard curve, drug loading, and encapsulation efficiency of AST in aqueous solution.

In vitro Release Analysis of Drug-Loaded Nanoparticles

The prepared drug-loaded nanoparticles were placed in a 3500KD dialysis bag and stirred at 200 r/s in a pH 7.2 buffer solution (37°C). At different time points, 1 mL of the dialysis buffer was collected, and the same volume and pH of the drug-release medium was added to the system before pouring the solution back into the buffer to continue the release experiment. The absorbance of the samples collected at different time points was measured using a UV-Vis spectrophotometer. The amount of released luteolin was calculated using a standard curve. Finally, the cumulative release profile of NP-Lut was plotted to assess its release behavior. The same procedure was used to NPs-AST release analysis.

Cytotoxicity Assay and Blood Compatibility Assessment

RAW264.7 macrophages, along with vascular endothelial cells, were purchased from the Cell Bank of the Chinese Academy of Sciences (Shanghai, China). RAW264.7 macrophages were cultured with complete Dulbecco's Modified Eagle's Medium (DMEM) medium containing 10% FBS and endothelial cell medium (ECM) at 37 °C in 5% CO2, respectively. All the cells were regularly checked for mycoplasma contamination. RAW264.7 macrophages was seeded in 96-well plates at a density of 1.0×10^4 cells/well. The cells were incubated with 100 μL of fresh complete medium containing various concentrations of NPs-Lut or NPs-AST for another 24 h. Then, the medium was replaced with fresh complete medium. A volume of 10 μL of CCK-8 reagent was added to each well and incubated for 2 h. Then, 100 μL supernatant from each well was transferred to a 96-well plate. The adsorption measurements were recorded at 450 nm using a microplate reader. Data processing was performed using GraphPad Prism software. For calcein-AM and PI double staining assay, macrophages were cultured using DMEM medium containing various concentrations of NPs for 24 h, subsequently being treated with calcein-AM (5 μg/mL) and PI (5 μg/mL) for another 30 minutes. After washing with PBS, the macrophages were carried out for the inverted fluorescence microscope imaging. Besides, macrophages treated with different concentrations of NPs-Lut were harvested and performed the double staining of PI and Annexin V-FITC. The obtained results were analyzed using flow cytometry with flowjo research software. For the hemolysis assay, blood from C57BL/6J mice was centrifuged at 3000 rpm and washed with PBS buffer for 6 times to obtain pure erythrocytes. 150 μL of erythrocytes (4%, v/v) was mixed with the same volume of distilled water, PBS buffer and PBS solution containing different concentrations of NPs-Lut, respectively. After 8 h of incubation, the mixtures were centrifuged to spin down erythrocytes and the obtained supernatants were measured with the adsorption of 540 nm via the microreader. Hemolysis rate was calculated According to the equation (3), in which I was the adsorption intensity of the erythrocytes incubated with NPs-Lut solutions while I_0 is the adsorption intensity of the erythrocytes in distilled water.

$$Hemolysis\,(\%) \;=\; (I/I_0) * 100\% \tag{3}$$

In vivo Animal Experimentation

Ethical Compliance and Experimental Animals $ApoE^{-/-}$ mice are derived from C57BL/6J mice with the apolipoprotein E gene knocked out. They are commonly used in studies on the pathogenesis of atherosclerosis and therapeutic drugs. Thirty-six 6-week-old male $ApoE^{-/-}$ mice (specific pathogen-free, SPF) and 6 age-matched male C57BL/6J mice, weighing 20–25 g, were provided by Beijing Wei tong Lihua Experimental Animal Technology Co., Ltd. The mice were housed in a 10,000-class clean barrier system, with environmental conditions controlled at a temperature of 20–26°C and humidity of 40%-70%. They were kept in IVC cages with autoclaved bedding, having ad libitum access to standard rodent feed and drinking water. Strict disinfection procedures for personnel and items were strictly enforced. The $ApoE^{-/-}$ mice were fed a high-fat diet for 16 weeks and then randomly divided into 6 groups (n=6): normal saline group (NS group), nanoparticle group (NPs group), atorvastatin group (AST group), luteolin group (Lut group), atorvastatin-loaded nanoparticle group (NPs-AST group), and luteolin-loaded nanoparticle group (NPs-Lut group). The interventions were administered via tail vein injection for 10 weeks at the following doses: 0.9% normal

saline, 2 mg/kg/day NPs, 3 mg/kg/day AST, 3 mg/kg/day NPs-AST, and 1.5 mg/kg/day NPs-Lut, respectively. All animal experiments in this study adhered to the National Institutes of Health (NIH) Guidelines for the Use of Animals in Research. The use of experimental animals was approved by the Experimental Animal Ethics Committee of Xuzhou Medical University (approval number: 202503T020). The high-fat diet was processed and prepared by Beijing Wei tong Lihua Experimental Animal Technology Co., Ltd., with the formula as follows: 2% cholesterol, 8% egg yolk powder, 10% lard, 0.2% bile salt, and 80% basal diet (accounting for the remaining proportion). Finally, euthanize the mice with excessive CO_2.

Establishment of Vulnerable AS Model Mice

To establish the animal models of VAPs, $ApoE^{-/-}$ mice, were employed. 6-week-old mice were adaptively fed for 7 days and then continuously fed with a high-fat diet for 16 weeks. After 4 months of HFD feeding, the whole aorta was harvested to confirm the formation of VAPs in HFD mice. Meanwhile, the frozen sections of the aortic arch (n = 3) were treated with Hematoxylin-eosin (HE) staining, Masson's trichrome staining, and oil red O staining, respectively, validating the presence of the formation hallmarks of VAPs.

In vivo Biocompatibility Assessment

Healthy C57BL/6J mouse was administered intravenously with saline and NPs-Lut solution (3 mg/kg/day; 2-folder higher concentration than that used for AS treatment) as same dosing frequency. At 0 d and 12 w, the blood serum was collected for biochemistry and blood routine examinations, and the main organs of mice were harvested for histopathological changes analysis, aiming at testifying long term toxicity of NPs-Lut.

Western Blotting

Information on the antibodies is provided in Table S1. Sample Aortic tissues were weighed and transferred into 1.5 mL EP tubes, then minced into small pieces. The tissue fragments were mixed with lysis buffer, fixed onto a tissue homogenizer, and homogenized thoroughly for 1 minute. The mixture was subsequently lysed on ice for 30 minutes, followed by centrifugation to obtain the supernatant. Protein concentrations in the supernatant were determined using a BCA Protein Assay Kit according to the manufacturer's instructions. Samples were adjusted to equal protein concentrations before being subjected to SDS-PAGE gel electrophoresis for separation. Proteins were then electrophoretically transferred onto PVDF membranes for immunoblot analysis. The PVDF membranes were blocked with 5% skimmed milk in blocking buffer by gentle shaking on a rocking platform at room temperature for 2 hours. After blocking, membranes were incubated with primary antibodies overnight at 4°C. The next day, following washing, membranes were exposed to ECL working solution, gently agitated to ensure uniform contact with the detection reagent, and then placed on a detection plate. Protein signals were visualized and photographed using an ECL chemiluminescence imaging system. Exported images were subjected to semi-quantitative analysis using ImageJ software.

QRT-PCR

The primers we designed are as follows:

GAPDH: F 5′-GAGAGGGAAATCGTGCGT-3′, R 5′-GGAGGAAGAGGATGCGG-3′;

GRP78: F 5′-CTCCGGCGTGAGGTAGAAAA-3′, R 5′-AGAGCGGAACAGGTCCATGT-3′;

CHOP: F 5′-AGGAGGTCCTGTCCTCAGATGA-3′, R 5′-ATGTGCGTGTGACCTCTGTTG-3′;

caspase12: F 5′-CTCAAAGAAGTGCGGACCCTCAAG-3′, R 5′-TCGGCTGTCTCTGCTCCATTCC-3′. Detection of GPR78, CHOP, and caspase12 mRNA Expression in aorta. This section focuses on the isolation and quantification of mRNA from aortic tissue. Total RNA was extracted using Trizol reagent according to standard protocols, and complementary DNA (cDNA) was synthesized via reverse transcription. Quantitative real-time PCR (qRT-PCR) was then conducted using specific primers targeting GRP78, CHOP, and caspase-12. All additional procedures were performed in strict accordance with the respective manufacturer's guidelines.

Statistical Analysis

Data are presented as the mean ± standard deviation (mean ± SD). All experiments were conducted with at least three biological replicates ($n \geq 3$). Comparisons between two groups were performed using Student's *t*-test, while comparisons among three or more groups were assessed using one-way analysis of variance (ANOVA). Statistical analyses and graphical representations were carried out using GraphPad Prism 8. A p value < 0.05 was considered statistically significant.

Results and Discussion

Synthesis and Characterization of NPs-Lut and NPs-AST

The presence of abundant mesopores and a robust structural framework is essential for achieving sustained drug release.[35–38] In this study, an amino-functionalized hollow mesoporous silica (HMS) nanoparticle with a highly porous architecture was successfully synthesized using a previously established protocol.[34] As shown in the TEM and SEM images (Figure 1A and B), the particles exhibited a uniform spherical morphology with an average diameter of approximately 250 nm. The excellent drug-loading capability of the HMS platform has been demonstrated in previous work.[34]

To enable specific targeting, the sulfhydryl (-SH) groups of the osteopontin (OPN) antibody were activated using dithiothritol (DTT), and the amino ($-NH_2$) groups on the HMS carrier were covalently linked via the heterobifunctional crosslinker succinimide 4-(n−maleimide methyl) cyclohexane-1-carboxylate (SMCC). The OPN antibody was then stably conjugated to the carrier surface, resulting in NPs endowed with OPN-targeting functionality.

Subsequently, the engineered nanoparticles were incubated with luteolin or AST solutions under reduced pressure and continuous stirring at 4 °C. After centrifugation and subsequent lyophilization, the drug-loaded formulations—NPs-Lut and NPs-AST—were successfully obtained as dry powders.

Dynamic light scattering (DLS) analysis revealed that the hydrodynamic diameter of NPs-Lut remained within the range of 240–250 nm, suggesting that drug loading did not significantly alter particle size (Figure 1C). Zeta potential measurements showed a shift from −11.05 to −12.56 mV for free luteolin from −15.01 to −16.35 mV for NPs-Lut, confirming successful drug encapsulation. A similar trend was observed for NPs-AST, although NPs-Lut exhibited a more pronounced negative surface potential (Figure 1D), likely contributing to improved colloidal stability.

Drug loading content (DLC) and encapsulation efficiency (EE) were quantitatively evaluated as critical indicators of the nanocarrier's drug-loading performance. Luteolin showed excellent linear relationships between absorbance and concentration in aqueous solution (Figure 1E). At a luteolin concentration of 0.300 mg mL^{-1}, the EE reached 88.25%, and the DLC was 52.08%, representing the optimal formulation (Figure 1F). Similarly, AST showed excellent linear relationships between absorbance and concentration in aqueous solution too (Figure 1G), and the EE and DLC at the same concentration were 89.17% and 50.10%, respectively (Figure 1H). These results collectively indicate that the developed NPs exhibit high drug-loading capacity and efficiency, rendering them promising candidates for targeted therapeutic delivery.

In vitro Drug Release of NPs-Lut and NPs-AST

The in vitro drug release profiles revealed a sustained and controlled release behavior for both NPs-Lut and NPs-AST. For NPs-Lut, the cumulative drug release reached 5.03% within the first 0.5 h, 55.76% at 12 h, and 63.17% at 24 h, with the release curve gradually plateauing thereafter (Figure 1I). Similarly, for NPs-AST, cumulative release was 5.67% within the first 0.5 h, 56.32% at 12 h, and 64.04% at 24 h, also demonstrating a steady and controlled release profile (Figure 1J). Importantly, no burst release was observed for either formulation, indicating the excellent structural stability of the nanoparticles and their capacity for sustained drug release.

In vitro Cytotoxicity Assays and Hemocompatibility of NPs-Lut

The cytotoxicity and hemocompatibility of NPs-Lut are crucial parameters for their safe application in vivo. To evaluate the cytotoxicity and biocompatibility of NPs-Lut, we first assessed cell viability of macrophages and endothelial cells treated with varying concentrations of the drug (0, 12.5, 25, 50, 75, 100, and 125 μg/mL) using the CCK-8 assay. The results showed that at the highest tested concentration of 125 μg/mL, cell viability for both cell

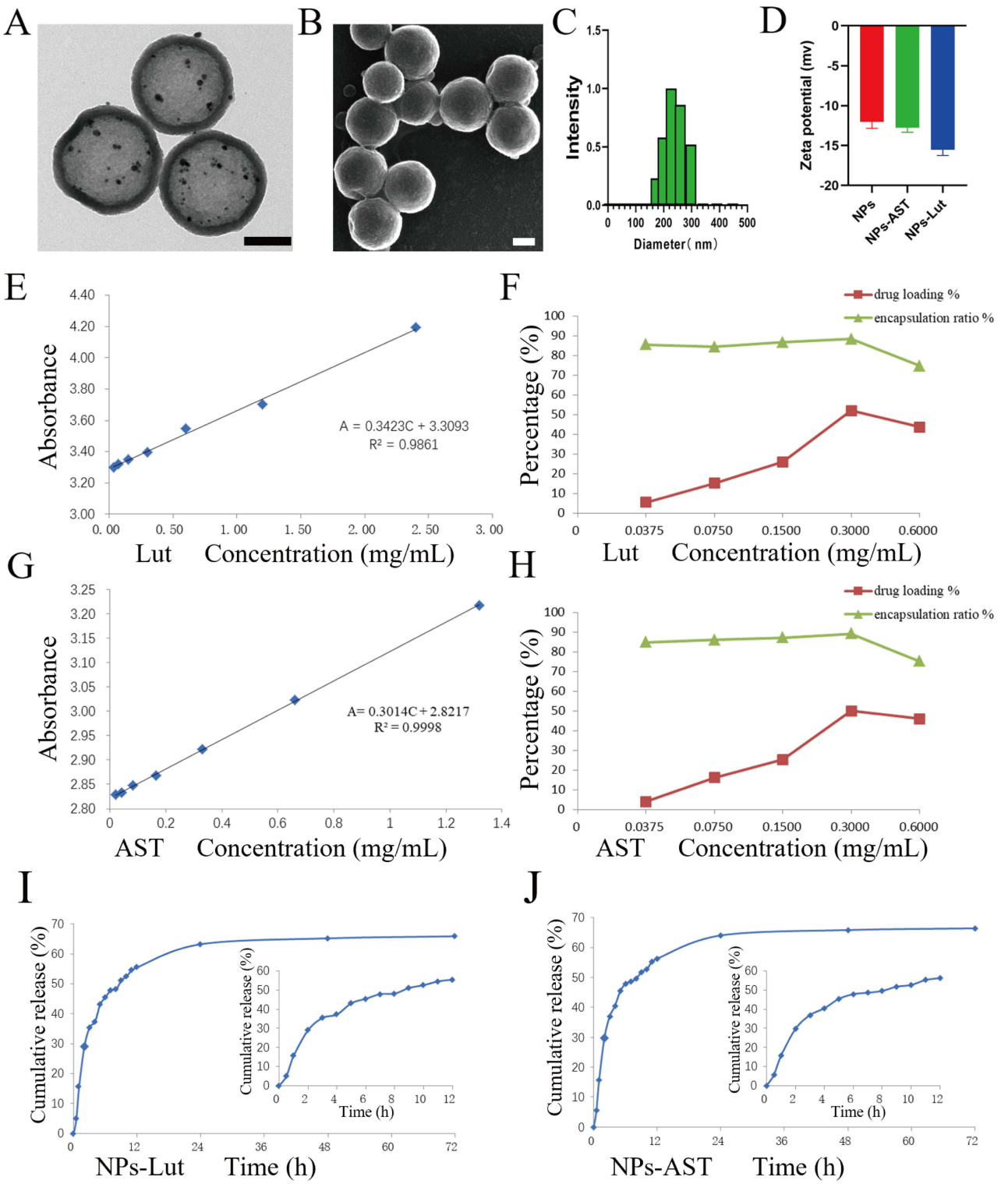

Figure 1 Characterizations and Properties of NPs-Lut and NPs-AST Nanoparticle Formulations. (**A**) TEM observation of NPs, scale bar: 100 nm; (**B**) SEM observation of NPs, scale bar: 100 nm; (**C**) The hydrodynamic diameter of NPs-Lut Nanoparticles; (**D**) Zeta potentials of NPs, NPs-AST and NPs-Lut; (**E**) The linear relationship between the concentration of luteolin in aqueous solution and the absorbance; (**F**) The drug loading capacity and encapsulation efficiency of NPs at different luteolin concentrations; (**G**) The linear relationship between the concentration of AST in aqueous solution and the absorbance; (**H**) The drug loading capacity and encapsulation efficiency of NPs at different AST concentrations; (**I**) In vitro drug release curve of NPs-Lut; (**J**) In vitro drug release curve of NPs-AST. (n = 3). Each bar in the graph represents the mean ± standard deviation.

https://doi.org/10.2147/IJN.S566896

types remained above 85% (Figure 2A). To directly observe the effect of NPs-Lut on cell survival and death, live/dead dual staining (Calcein AM/propidium iodide) was performed on macrophages. Notably, even at a concentration of 150 μg/mL, a high proportion of live cells was observed, with only a few dead cells detected, as evidenced by the predominance of green fluorescence (Figure 2B). To further confirm the cytocompatibility, flow cytometry analysis was conducted. Consistently, at a concentration of 125 μg/mL, macrophage viability exceeded 90% (Figure 2C), corroborating the previous assays. These results collectively demonstrate that the cytotoxicity of NPs-Lut is negligible. Furthermore, hemolysis assays were performed to evaluate the effect of NPs-Lut on red blood cells (RBCs) at different concentrations, using PBS and deionized water as negative and positive controls, respectively. Even at the highest concentration tested, NPs-Lut induced minimal hemolysis (<5%, Figure 2D), indicating excellent hemocompatibility. Taken together, these findings strongly support the high biocompatibility of NPs-Lut as a nano-drug delivery system for targeted therapy of VAPs.

Development of AS Model Mice and Assessment of VAPs

To establish an animal model of VAPs, apolipoprotein E double knockout C57BL/6J mice (ApoE$^{-/-}$) were used. Six-week-old mice were acclimated for 7 days, followed by continuous feeding with a high-fat diet (HFD) for 5 months. After 4 months of HFD feeding, vascular tissues from the heart and the aorta extending to the iliac arteries were collected (Figure 3A, left) to confirm the formation of VAPs. Oil Red O staining revealed lipid-rich lesion areas in the ApoE$^{-/-}$ mice, confirming the presence of VAPs (Figure 3A, right). Additionally, histological analyses of AS plaque sections were performed using hematoxylin and eosin (H&E), Masson's trichrome, and Oil Red O staining. As shown in Figure 3B, typical features of VAPs were observed in the aorta, including eccentric lipid necrotic cores, thin and rupture-prone fibrous caps, markedly reduced collagen fibers, and abundant lipid accumulation.

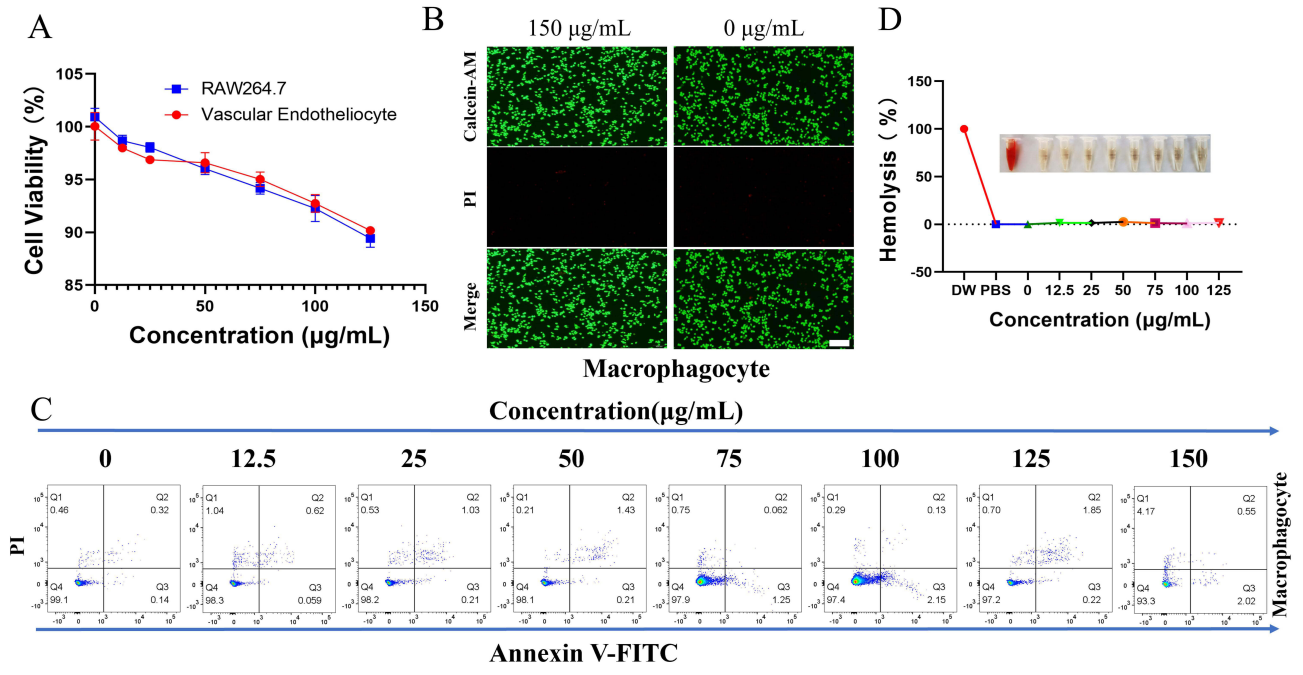

Figure 2 Cytotoxicity and biocompatibility of the NPs-Lut. (**A**) The viability of macrophages and endothelial cells after incubation with different concentrations of NPs-Lut was assessed using the CCK-8 assay; (**B**) CLSM images of Calcein-AM/PI costained macrophages after treatment with 0 and 150 μg/mL NPs-Lut. Green signal: live cells, red signal: dead cells. Scale bars are 100 μm; (**C**) The relative viability of macrophages treated with different concentrations of NPs-Lut was analyzed by flow cytometry. (**D**) The hemolysis rate of normal C57BL/6J mouse erythrocytes treated with different concentrations (0 to 125 μg/mL) of NPs-Lut. PBS was used as the negative control, and deionized water was used as the positive control; (n=3). Each bar in the graph represents the mean ± standard deviation.

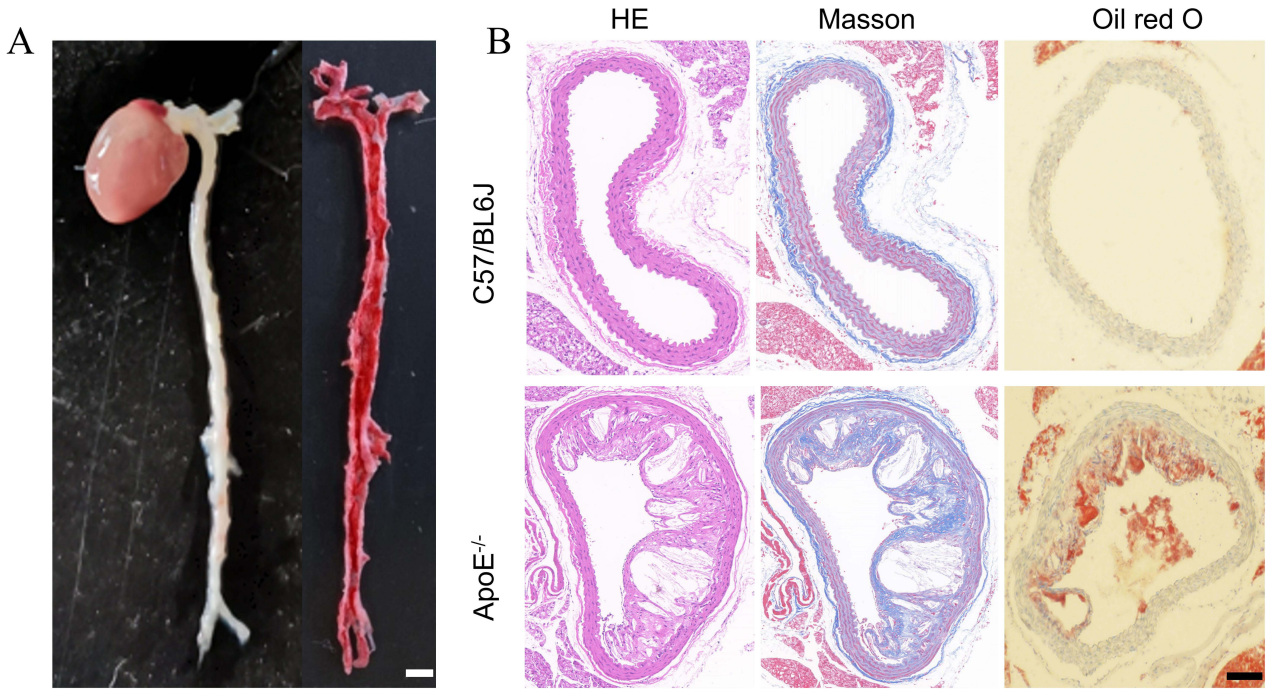

Figure 3 Construction and validation of a mouse model of VAPs. (**A**) Oil red O staining of the aorta from atherosclerosis (AS) model mice (left) and the stained aorta (right). The scale bar is 2 mm; (**B**) H&E, Masson, and Oil Red O staining were performed on aortic tissues from healthy C57BL/6J mice (upper) and AS model mice (lower). The scale bar is 200 μm. Each bar in the graph represents the mean ± standard deviation.

In vivo Changes in Serum Lipid Parameters

It is well established that dyslipidemia is an independent risk factor for atherosclerosis (AS).[2,17,39] The initiation of AS is generally attributed to the infiltration of lipid particles including low-density lipoprotein (LDL) particles into the vascular wall. Oxidized LDL (ox-LDL) is readily taken up by macrophage scavenger receptors, leading to the formation of foam cells. The excessive accumulation of foam cells increases the likelihood of plaque rupture in AS lesions. In our previous study, we demonstrated that luteolin could alleviate ox-LDL-induced lipid accumulation in macrophages in vitro.[40]

In the present study, we assessed the serum lipid profiles—total cholesterol (TC), triglycerides (TG), high-density lipoprotein cholesterol (HDL-C), and LDL-C in mice subjected to different treatments. As shown in Figure 4A, all treatment groups except the NS and NPs groups exhibited a significant reduction in TC levels, with luteolin showing a marked lipid-lowering effect, albeit slightly weaker than that of AST. Similar trends were observed for TG and LDL-C levels (Figure 4B and C). Interestingly, both NPs-Lut and NPs-AST demonstrated weaker lipid-lowering effects compared to free AST and luteolin. This may be attributed to the nanoparticle carriers facilitating targeted delivery of luteolin and AST to atherosclerotic plaques, thereby limiting the systemic exposure of the drugs and diminishing their systemic lipid-lowering activity. Notably, no significant differences were observed in HDL-C levels across all experimental groups (Figure 4D).

In vivo Changes in Serum Inflammatory Parameters

Inflammatory responses play a central role in the initiation and progression of VAPs.[41–44] Oxidative modification of LDL has long been recognized as a critical step in the pathogenesis of AS, mediated through complex inflammatory and immune mechanisms.[45–47] Regardless of the primary morphology of plaques, rupture or erosion of the intima at sites of thrombogenic AS is consistently characterized by inflammation. Targeted modulation of inflammation has been shown to reduce residual cardiovascular risk beyond LDL-C lowering, significantly slowing AS progression.[48–50]

Tumor necrosis factor-α (TNF-α) is a key pro-inflammatory cytokine implicated in AS development. Studies have demonstrated that TNF-α not only influences lipid metabolism but also promotes the synthesis of other inflammatory mediators, such as

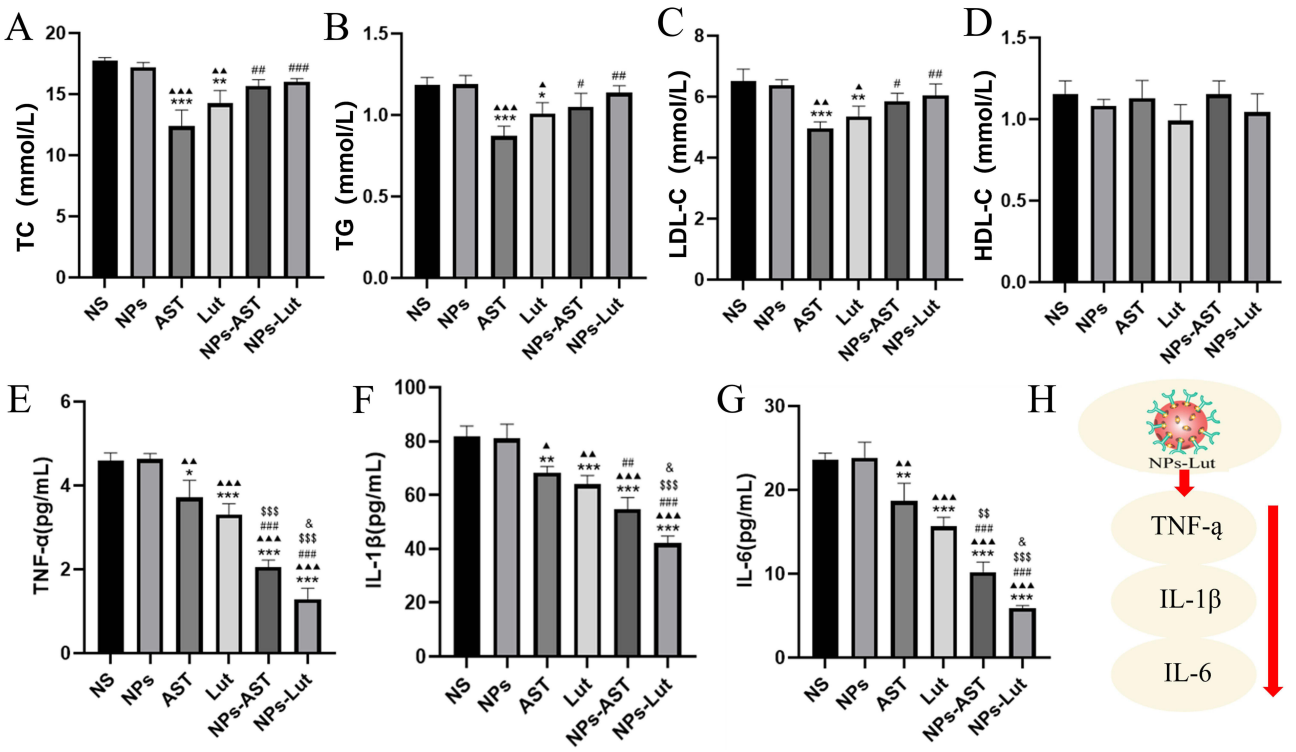

Figure 4 (**A**–**D**) represent serum TC, TG, LDL-C and HDL-C levels of mice in each group respectively; (**E**–**G**) showed serum TNF-α, IL-1β, IL-6 levels of mice in each group respectively; (**H**) Schematic diagram of NPs-Lut reducing inflammatory factors. * indicates p <0.05 compared with the NS group; ▲ indicates p <0.05 compared with the NPs group; # indicates p <0.05 compared with the AST group; & indicates p <0.05 compared with the NPs-AST group; $$ indicates p <0.01; $$$ indicates p <0.001, compared with the Lut group; ** indicates p <0.01; *** indicates p <0.001; ## indicates p <0.01; ### indicates p <0.001; ▲▲ indicates p <0.01; ▲▲▲ indicates p <0.001; and so on. (n=3). Each bar in the graph represents the mean ± standard deviation.

interleukin-1 (IL-1) and interleukin-8 (IL-8), thereby amplifying local inflammatory responses.[16] Additionally, TNF-α induces matrix metalloproteinase expression, leading to fibrous cap thinning and promoting plaque instability.[51]

Interleukin-1β (IL-1β) is another pivotal pro-inflammatory cytokine.[52] Cholesterol crystals have been demonstrated to induce macrophages to secrete IL-1β, thereby exacerbating intra-plaque inflammation. IL-1β not only amplifies inflammation by promoting the production of other pro-inflammatory cytokines but also contributes to macrophage recruitment.[53] Interleukin-6 (IL-6) further exacerbates the disease by inducing endothelial dysfunction, promoting vascular smooth muscle cell proliferation and migration, and recruiting and activating inflammatory cells.[54]

In this study, serum levels of TNF-α, IL-1β, and IL-6 were measured after 10 weeks of different interventions. As shown in Figure 4E, TNF-α levels were progressively reduced across the AST, luteolin, NPs-AST, and NPs-Lut groups, with significant differences observed among all groups. Notably, NPs-Lut exhibited the strongest inhibitory effect on TNF-α expression. A similar trend was observed for IL-1β and IL-6 levels (Figure 4F and G). These results demonstrate the potent anti-inflammatory effect of NPs-Lut in reducing TNF-α, IL-1β, and IL-6 levels (Figure 4H), with a statistically significant difference compared to the luteolin group ($P < 0.001$). These findings confirm the intrinsic anti-inflammatory activity of luteolin and, importantly, highlight the precise targeting capability of NPs-Lut in modulating inflammation at its source within AS plaques.

In vivo Treatment-Induced Pathological Changes in VAPs

To investigate the effects of different interventions on AS lesions in ApoE$^{-/-}$ mice, aortic root sections were harvested after 10 weeks of treatment and subjected to Oil Red O staining (Figure 5A). Quantification of plaque areas in the aortic root revealed no significant differences between the NPs group and the NS group. In contrast, both AST and luteolin treatments significantly reduced plaque areas compared to the NS group. Notably, there was no significant difference in plaque area

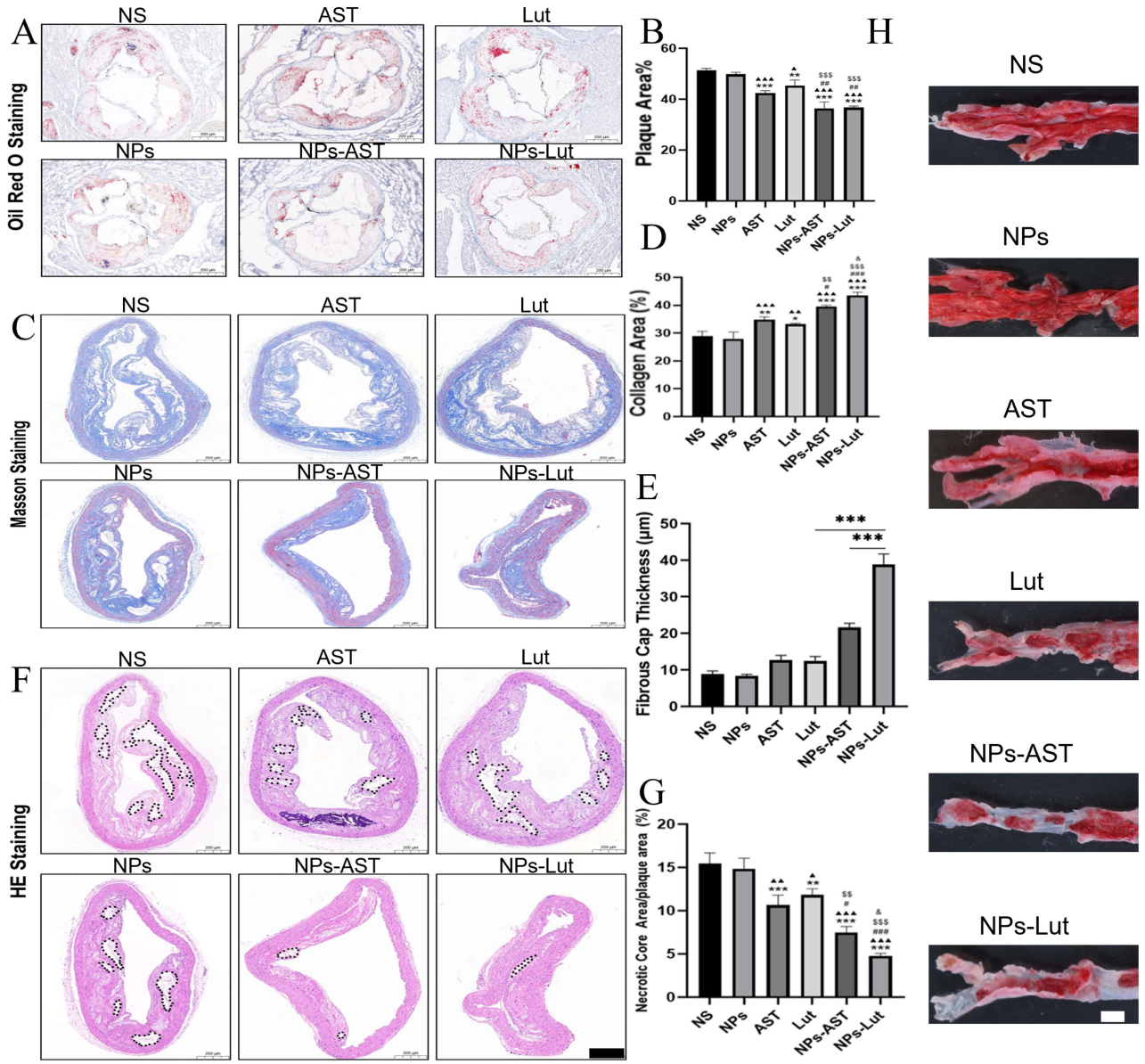

Figure 5 Histological analysis of changes in VAPs. (**A**) Oil red O staining of the aortic root in mice of different groups; (**B**) Quantitative analysis of aortic plaque area; (**C**) Masson staining of aortic arch tissues in mice of different groups; (**D**) Quantitative analysis of the area of plaque collagen fibril protein relative to the plaque area; (**E**) Quantitative analysis of fibrous cap thickness in VAPs of different groups; (**F**) HE staining of the aortic arch in mice of different groups; (**G**) Quantitative analysis of the necrotic core relative to the plaque area; (**H**) Gross Oil Red O staining of the abdominal aorta in mice of different groups. (n=3). Each bar in the graph represents the mean ± standard deviation. * indicates p <0.05 compared with the NS group; ▲ indicates p <0.05 compared with the NPs group; # indicates p <0.05 compared with the AST group; & indicates p <0.05 compared with the NPs-AST group; $$ indicates p <0.01; $$$ indicates p <0.001, compared with the Lut group; ** indicates p <0.01; ***indicates p <0.001; ## indicates p <0.01; ### indicates p <0.001; ▲▲indicates p <0.01; ▲▲▲ indicates p <0.001; and so on.

between the AST and Lut groups. Furthermore, both the NPs-AST and NPs-Lut groups showed a marked reduction in plaque area compared to the NS group, with no significant difference between NPs-AST and NPs-Lut groups (Figure 5B).

To assess plaque stability, a key determinant of vulnerability, Masson's trichrome staining was performed on aortic arch sections collected after 10 weeks of treatment (Figure 5C). Analysis of collagen fiber content within plaques showed no significant difference between the NPs and NS groups. However, collagen content was significantly increased in the AST, Lut, NPs-AST, and NPs-Lut groups compared to the NS group. While there was no significant difference between the AST and luteolin groups, both the NPs-AST and NPs-Lut groups exhibited markedly higher collagen content than the AST and Lut groups. Importantly, collagen content in the NPs-Lut group was significantly higher than that in the NPs-AST group (Figure 5D).

https://doi.org/10.2147/IJN.S566896

Fibrous cap thickness, another critical indicator of plaque stability, was also evaluated. The NS and NPs groups exhibited significantly thinner fibrous caps compared to the AST and luteolin groups. In contrast, fibrous cap thickness was markedly increased in the NPs-AST and NPs-Lut groups, with average thicknesses of approximately 20.6–22.8 μm and 35.7–41.3 μm, respectively. Remarkably, fibrous cap thickness in the NPs-Lut group was approximately 1.8 times greater than that in the NPs-AST group, having differences statistical (Figure 5E).

To assess changes in necrotic core area within plaques across treatment groups, hematoxylin and eosin (H&E) staining was performed on aortic root sections (Figure 5F). Quantitative analysis revealed no significant difference in necrotic core area between the NPs and NS groups. In contrast, the AST, luteolin, NPs-AST, and NPs-Lut groups exhibited a significant reduction in necrotic core area compared to the NS group. No significant difference was observed between the AST and luteolin groups. Notably, both the NPs-AST and NPs-Lut groups showed markedly reduced necrotic core areas, with the NPs-Lut group demonstrating a further significant reduction compared to the NPs-AST group (Figure 5G).

Finally, to provide a visual representation of plaque burden, Oil Red O staining was performed on abdominal aortas from each group (Figure 5H). The results clearly demonstrated that the NPs-Lut group exhibited the smallest plaque areas among all groups.

In vivo Treatment-Induced mRNA and Protein Expression of ERS and Apoptosis-Related Genes in Each Experimental Group

The endoplasmic reticulum (ER) not only serves as a critical site for free cholesterol-induced secretion of pro-inflammatory cytokines such as TNF-α and IL-6 in macrophages but also contributes to the induction of TNF-α production. ERS is a prominent feature of macrophages within human and murine AS lesions.[55] Glucose-regulated protein 78 (GRP78) plays a key regulatory role during ERS,[56] and its expression typically increases in response to ERS.

CHOP, a central node integrating signals from the three canonical ERS pathways (pERK, ATF6, and IRE1), is a critical mediator linking ERS to apoptosis.[57] Under physiological conditions, CHOP is minimally expressed in the cytoplasm; however, during ERS, the dissociation of BiP/GRP78 from ER transmembrane proteins such as pERK and ATF6α leads to CHOP activation.[58] Caspase-12, located in the ER, is a key initiator of ERS-dependent apoptosis,[59] triggering caspase cascades and pERK-CHOP-Bax–mediated mitochondrial apoptotic pathways. Additionally, CHOP overexpression can downregulate anti-apoptotic Bcl-2, facilitating Bax translocation from the cytosol to mitochondria and triggering mitochondrial-dependent apoptosis. Therefore, assessing ERS-related protein expression provides valuable insights into ERS-induced apoptosis.

In this study, following 10 weeks of treatment, we evaluated the expression of ERS and apoptosis-related genes and proteins within VAPs of $ApoE^{-/-}$ mice.

For GRP78 mRNA, no significant differences were observed between the NPs and NS groups. However, GRP78 mRNA levels were significantly reduced in the AST, luteolin, NPs-AST and NPs-Lut groups compared to the NS group. No significant difference was noted between the AST and Lut groups. Notably, both the NPs-AST and NPs-Lut groups exhibited further reductions in GRP78 mRNA expression, with the NPs-Lut group showing a more pronounced decrease than the NPs-AST group (Figure 6A). Similarly, GRP78 protein levels showed no significant changes in the NPs group relative to the NS group, while they were significantly decreased in the AST, luteolin, and NPs-AST groups. No difference was found between the AST and luteolin groups. Both NPs-AST and NPs-Lut groups showed further reductions in GRP78 protein expression, with the NPs-Lut group exhibiting the most substantial decrease (Figure 6B and C).

For CHOP mRNA, no significant difference was observed between the NS and NPs groups. However, CHOP mRNA expression was markedly reduced in the AST, luteolin, NPs-AST, and NPs-Lut groups compared to the NS group. No significant difference was found between the AST and luteolin groups. Both the NPs-AST and NPs-Lut groups demonstrated further reductions, with the NPs-Lut group showing the lowest CHOP mRNA levels (Figure 6D). Consistently, CHOP protein levels followed a similar trend: no significant difference between NS and NPs groups, while AST, luteolin, and NPs-AST groups showed significant reductions. No difference was observed between the AST

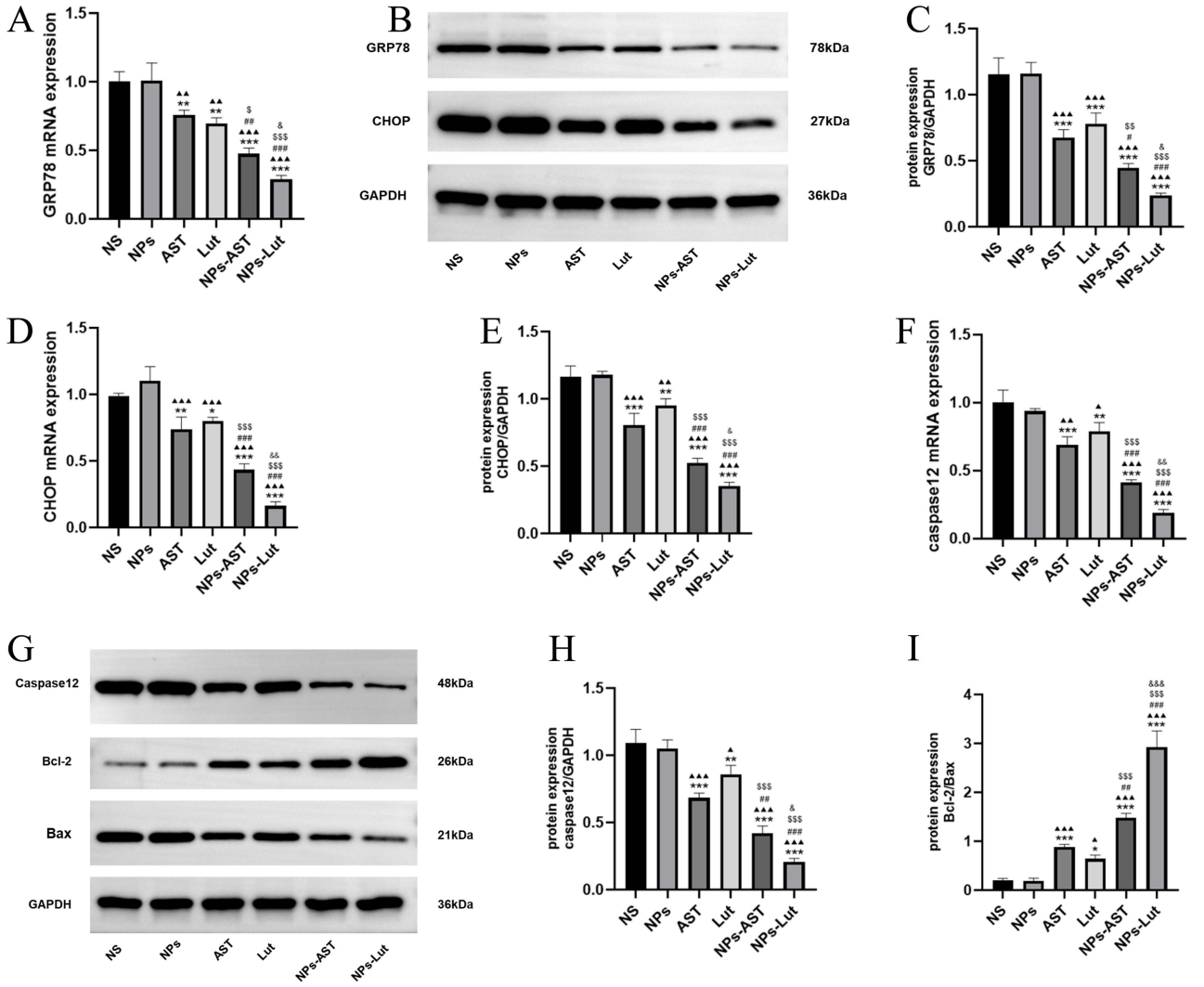

Figure 6 mRNA and protein expression levels of ERS and apoptosis-related proteins in each experimental group. (**A**) represent the expression level of GRP78 mRNA; (**B**) WB images showing the grayscale of ERS-related proteins among different groups; (**C**) Quantitative analysis of GRP78 protein expression levels; (**D**) represent the expression level of CHOP mRNA; (**E**) Quantitative analysis of CHOP protein expression levels; (**F**) represent the expression level of Caspase12 mRNA; (**G**–**I**) represent the expression level of apoptosis-related proteins. (n=3). Each bar in the graph represents the mean ± standard deviation. * indicates p <0.05 compared with the NS group; ▲ indicates p <0.05 compared with the NPs group; # indicates p <0.05 compared with the AST group; & indicates p <0.05 compared with the NPs-AST group; $$ indicates p <0.01; $$$ indicates p <0.001, compared with the Lut group; ** indicates p <0.01; ***indicates p <0.001; ## indicates p <0.01; ### indicates p <0.001; && indicates p <0.01; &&& indicates p <0.001; ▲▲indicates p <0.01; ▲▲▲ indicates p <0.001; and so on.

and luteolin groups. Both NPs-AST and NPs-Lut groups showed further reductions in CHOP protein expression, with NPs-Lut exhibiting the greatest suppression (Figure 6B and E).

For caspase-12 mRNA, no significant difference was observed between NS and NPs groups, while AST, luteolin, NPs-AST and NPs-Lut groups showed significant reductions. No difference was observed between AST and luteolin groups. Notably, NPs-AST and NPs-Lut groups showed further reductions in caspase-12 mRNA, with NPs-Lut demonstrating a greater decrease than NPs-AST (Figure 6F). At the caspase-12 protein level, no significant difference was observed between NS and NPs groups, whereas AST, luteolin, NPs-AST and NPs-Lut groups showed significant reductions. No difference was observed between AST and luteolin groups. Both NPs-AST and NPs-Lut groups exhibited further reductions, with NPs-Lut showing the greatest suppression (Figure 6G and H).

Regarding the Bcl-2/Bax ratio, no significant difference was observed between NS and NPs groups. In contrast, the AST, luteolin, NPs-AST and NPs-Lut groups demonstrated significant increases in the Bcl-2/Bax ratio. No difference was

https://doi.org/10.2147/IJN.S566896

observed between the AST and luteolin groups. Both NPs-AST and NPs-Lut groups showed further increases, with the NPs-Lut group exhibiting the highest Bcl-2/Bax ratio (Figure 6G and I).

Collectively, these findings demonstrate that NPs-Lut effectively suppresses ERS and apoptosis in VAPs, outperforming NPs-AST in modulating ERS-associated apoptotic pathways.

Body Weight and Biosafety Evaluation of NPs-Lut in ApoE$^{-/-}$ Mice

To further assess the biosafety of NPs-Lut, especially at double the standard dosage, we performed comprehensive hematological and biochemical analyses. Key parameters included liver function markers alanine aminotransferase (ALT), aspartate aminotransferase (AST), renal function indicators blood urea nitrogen (BUN), creatinine (CREA), cardiac enzymes creatine kinase (CK), lactate dehydrogenase (LDH), and hematological variables white blood cells (WBC), red blood cells (RBC), platelets (PLT), and hemoglobin (HGB). Notably, there were no significant changes in these indices two weeks after the end of treatment compared to baseline levels (Figure 7A). Throughout the treatment period, the body weights of mice in each group were meticulously monitored. No significant differences in body weight were observed among the groups before and after treatment (Figure 7B). These findings suggest that NPs-Lut administration did not induce significant hepatotoxicity, nephrotoxicity, or systemic adverse effects. Histological evaluations further supported the biosafety profile of NPs-Lut. No significant morphological or histopathological abnormalities were observed in major organs, including the heart, liver, spleen, lung, and kidney (Figure 7C). This favorable safety profile is likely attributable to the excellent targeting capability of the NPs, which effectively deliver luteolin to atherosclerotic plaques while sparing healthy tissues from off-target effects. Collectively, these results underscore the potential of NPs-Lut as a precise, safe, and effective nanotherapeutic for the targeted treatment of VAPs, paving the way for its future clinical application.

Due to the inherent hydrophobicity of luteolin caused by its hydrophobic moieties, luteolin suffers from poor aqueous solubility, rapid metabolism, a short half-life, low bioavailability, and suboptimal therapeutic efficacy, which factors have

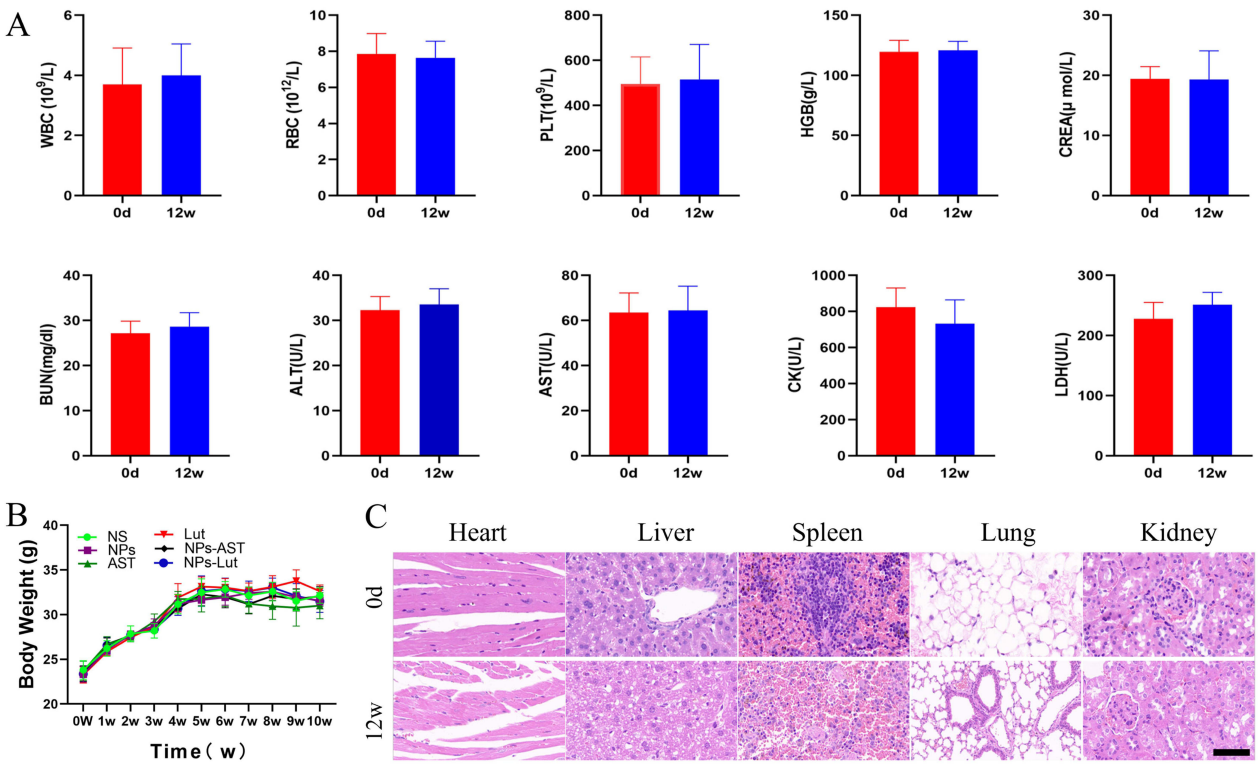

Figure 7 In vivo evaluation of biosafety. (**A**) Changes in blood indices of normal C57BL/6J mice before and after administration of NPs-Lut at a dose of 3 mg/kg/day; (**B**) Changes in body weight of mice in each experimental group before and after treatment; (**C**) Pathological observation of major organs in normal C57BL/6J mice before and after administration of NPs-Lut at a dose of 3 mg/kg/day, scale bar: 200 μm. (n=6). Each bar in the graph represents the mean ± standard deviation.

significantly limited its clinical application. This also accounts for the paucity of research regarding luteolin's targeted therapy for VAPs. Therefore, based on previous research, we took the lead in conducting a study on the targeted therapy of VAPs with luteolin. In our study, Pharmacodynamic data demonstrated that luteolin and the reference compound AST exhibited notable lipid-lowering effects (LDL-C reduction: 17.5% vs 23.7%; total cholesterol reduction: 19.6% vs 30.2%; triglyceride reduction: 14.0% vs 26.3%) differences may be attributed to disparities in bioavailability. Importantly, in terms of improving the stability of VAPs, the NPs-Lut achieved markedly superior therapeutic outcomes to non-targeted formulations (plaque area reduction: 28.4% vs 11.5%, $P < 0.01$). Notably, NPs-Lut demonstrated exceptional performance in enhancing plaque stability by suppressing pro-inflammatory cytokines TNF-α, IL-1β, and IL-6 while promoting collagen synthesis, NPs-Lut treatment resulted in a 150% increase in fibrous cap thickness and a 35.9% reduction in necrotic core area compared to NPs-AST.

Mechanistic investigations revealed that the therapeutic advantages of NPs-Lut were attributable to its dual regulatory effects: (1) a targeted, sustained release within the plaque microenvironment via nanoparticle-mediated delivery, and (2) attenuation of ERS by downregulating GRP78 and CHOP expression, thereby reducing macrophage apoptosis. Furthermore, the biosafety profile of NPs-Lut was rigorously validated by liver and kidney function tests, hematological analyses, and histopathological evaluations of major organs, collectively supporting its translational potential for precise therapy of VAPs in clinical settings.

Conclusion

In this study, we successfully developed a targeted nanodrug delivery system, NPs-Lut, providing a breakthrough strategy for the precise treatment of VAPs. The active targeting capability of NPs to VAPs was comprehensively validated through both in vitro and in vivo experiments, enabled by rational molecular modifications.[34] For the first time, we overcame the inherent limitations of the natural compound luteolin, including its low aqueous solubility and poor bioavailability, achieving precise accumulation and sustained release of luteolin within the lipid-rich and structurally complex core regions of VAPs.

Collectively, NPs-Lut holds great promise as a next-generation candidate for the precision treatment of vulnerable plaques, owing to its superior targeting efficiency, potent therapeutic efficacy, and favorable safety profile. These findings lay a solid foundation for the translational potential of NPs-Lut, warranting further in-depth investigations toward clinical application.

Data Sharing Statement

The data that support the findings of this study are available from the corresponding author upon reasonable request.

Acknowledgments

The authors would like to express their gratitude to the teachers and experimental platforms of the Institute of Cardiovascular Diseases of Xuzhou Medical University, the Department of Cardiology of the Affiliated Hospital of Xuzhou Medical University, and the Second Affiliated Hospital of Chongqing Medical University for their support and assistance throughout the entire experimental process.

Disclosure

The authors declare no conflicts of interest in this work.

References

1. Swirski FK, Nahrendorf M. Leukocyte behavior in atherosclerosis, myocardial infarction, and heart failure. *Science*. 2013;339(6116):161–166. doi:10.1126/science.1230719
2. Peng X, Lian Z, O'Brien V, et al. Foamy monocytes and atherogenesis in mice with combined hyperlipidemia and effects of antisense knockdown of apoCIII. *J Lipid Res*. 2025;66(4):100763. doi:10.1016/j.jlr.2025.100763
3. Pan Y, Jing J, Cai X, et al. Prevalence and vascular distribution of multiterritorial atherosclerosis among community-dwelling adults in Southeast China. *JAMA Network Open*. 2022;5(6):e2218307. doi:10.1001/jamanetworkopen.2022.18307
4. Christensen DM, Schjerning AM, Smedegaard L, et al. Long-term mortality, cardiovascular events, and bleeding in stable patients 1 year after myocardial infarction: a Danish nationwide study. *Eur Heart J*. 2023;44(6):488–498. doi:10.1093/eurheartj/ehac667

5. Khambhati J, Engels M, Allard-Ratick M, Sandesara PB, Quyyumi AA, Sperling L. Immunotherapy for the prevention of atherosclerotic cardiovascular disease: promise and possibilities. *Atherosclerosis*. 2018;276:1–9. doi:10.1016/j.atherosclerosis.2018.07.007
6. Ahmadi A, Argulian E, Leipsic J, Newby DE, Narula J. From subclinical atherosclerosis to plaque progression and acute coronary events: JACC state-of-the-art review. *J Am Coll Cardiol*. 2019;74(12):1608–1617. doi:10.1016/j.jacc.2019.08.012
7. Davies PF. Endothelial mechanisms of flow-mediated athero-protection and susceptibility. *Circ Res*. 2007;101(1):10–12. doi:10.1161/CIRCRESAHA.107.156539
8. Libby P. The changing landscape of atherosclerosis. *Nature*. 2021;592(7855):524–533. doi:10.1038/s41586-021-03392-8
9. Puylaert P, Zurek M, Rayner KJ, De Meyer GRY, Martinet W. Regulated necrosis in atherosclerosis. *Arterioscler Thromb Vasc Biol*. 2022;42(11):1283–1306. doi:10.1161/ATVBAHA.122.318177
10. Custodis F, Baumhäkel M, Schlimmer N, et al. Heart rate reduction by ivabradine reduces oxidative stress, improves endothelial function, and prevents atherosclerosis in apolipoprotein E-deficient mice. *Circulation*. 2008;117(18):2377–2387. doi:10.1161/CIRCULATIONAHA.107.746537
11. Zheng SL, Roddick AJ. Association of aspirin use for primary prevention with cardiovascular events and bleeding events: a systematic review and meta-analysis. *JAMA*. 2019;321(3):277–287. doi:10.1001/jama.2018.20578
12. Ruotsalainen AK, Mäkinen P, Ylä-Herttuala S. Novel RNAi-based therapies for atherosclerosis. *Curr Atheroscler Rep*. 2021;23(8):45. doi:10.1007/s11883-021-00938-z
13. Banach M, Penson PE, Farnier M, et al. Bempedoic acid in the management of lipid disorders and cardiovascular risk. 2023 position paper of the International Lipid Expert Panel (ILEP). *Prog Cardiovasc Dis*. 2023;79:2–11. doi:10.1016/j.pcad.2023.03.001
14. Lennernäs H. Clinical pharmacokinetics of atorvastatin. *Clin Pharmacokinet*. 2003;42(13):1141–1160. doi:10.2165/00003088-200342130-00005
15. Wang L, Wang M, Niu H, et al. Cholesterol-induced HRD1 reduction accelerates vascular smooth muscle cell senescence via stimulation of endoplasmic reticulum stress-induced reactive oxygen species. *J Mol Cell Cardiol*. 2024;187:51–64. doi:10.1016/j.yjmcc.2023.12.007
16. Koga JI, Umezu R, Kondo Y, et al. Cyclophilin D induces necrotic core formation by mediating mitochondria-associated macrophage death in advanced atherosclerotic lesions. *Atherosclerosis*. 2024;396:118524. doi:10.1016/j.atherosclerosis.2024.118524
17. Yusuf S, Hawken S, Ounpuu S, et al. Effect of potentially modifiable risk factors associated with myocardial infarction in 52 countries (the INTERHEART study): case-control study. *Lancet*. 2004;364(9438):937–952. doi:10.1016/S0140-6736(04)17018-9
18. De Meyer GRY, Zurek M, Puylaert P, Martinet W. Programmed death of macrophages in atherosclerosis: mechanisms and therapeutic targets. *Nat Rev Cardiol*. 2024;21(5):312–325. doi:10.1038/s41569-023-00957-0
19. Shi Z, Huang J, Chen C, Zhang X, Ma Z, Liu Q. Lipid nanoparticles encapsulating curcumin for imaging and stabilization of vulnerable atherosclerotic plaques via phagocytic "eat-me" signals. *J Control Release*. 2024;373:265–276. doi:10.1016/j.jconrel.2024.07.027
20. Nadalin P, Kim JK, Park SU. Recent insights into luteolin and its biological and pharmacological activities. *EXCLI J*. 2024;23:787–794. doi:10.17179/excli2024-7168
21. Theoharides TC, Cholevas C, Polyzoidis K, Politis A. Long-COVID syndrome-associated brain fog and chemofog: luteolin to the rescue. *BioFactors*. 2021;47(2):232–241. doi:10.1002/biof.1726
22. Gendrisch F, Esser PR, Schempp CM, Wölfle U. Luteolin as a modulator of skin aging and inflammation. *BioFactors*. 2021;47(2):170–180. doi:10.1002/biof.1699
23. Aziz N, Kim MY, Cho JY. Anti-inflammatory effects of luteolin: a review of in vitro, in vivo, and in silico studies. *J Ethnopharmacol*. 2018;225:342–358. doi:10.1016/j.jep.2018.05.019
24. Chen L, Chang S, Zhao L, et al. Biosynthesis of a water solubility-enhanced succinyl glucoside derivative of luteolin and its neuroprotective effect. *Microb Biotechnol*. 2022;15(9):2401–2410. doi:10.1111/1751-7915.14095
25. Lv J, Song X, Luo Z, Huang D, Xiao L, Zou K. Luteolin: exploring its therapeutic potential and molecular mechanisms in pulmonary diseases. *Front Pharmacol*. 2025;16:1535555. doi:10.3389/fphar.2025.1535555
26. Fu QT, Zhong XQ, Chen MY, et al. Luteolin-loaded nanoparticles for the treatment of melanoma. *Int J Nanomed*. 2023;18:2053–2068. doi:10.2147/IJN.S400329
27. Chang XQ, Yue RS. Therapeutic potential of luteolin for diabetes mellitus and its complications. *Chin J Integr Med*. 2025;31(6):566–576. doi:10.1007/s11655-024-3917-z
28. Song K, Zhou L, Wang C, et al. Novel luteolin@pro-phytomicelles: in vitro characterization and in vivo evaluation of protection against drug-induced hepatotoxicity. *Chem Biol Interact*. 2022;365:110095. doi:10.1016/j.cbi.2022.110095
29. Li R, Zheng Y, Li X, et al. Hyaluronic acid-modified luteolin-copper complex nanodelivery system for bacterial prostatitis. *ACS omega*. 2024;9(41):42582–42592. doi:10.1021/acsomega.4c07724
30. Wu S, Wang ST, Chen GY, et al. Monophosphate derivatives of luteolin and apigenin as efficient precursors with improved oral bioavailability in rats. *Antioxidants*. 2024;13(12):1530. doi:10.3390/antiox13121530
31. Banerjee A, Mal S, Roy P, Chatterji U. Regulating environmental arsenic-mediated gut-brain toxicity using chitosan-conjugated luteolin gold nanoparticles. *Ecotoxicol Environ Saf*. 2025;297:118250. doi:10.1016/j.ecoenv.2025.118250
32. Bi X, Peng H, Xiong H, et al. Fabrication of the rapid self-assembly hydrogels loaded with luteolin: their structural characteristics and protection effect on ulcerative colitis. *Foods*. 2024;13(7):1105. doi:10.3390/foods13071105
33. Mitchell MJ, Billingsley MM, Haley RM, Wechsler ME, Peppas NA, Langer R. Engineering precision nanoparticles for drug delivery. *Nat Rev Drug Discov*. 2021;20(2):101–124. doi:10.1038/s41573-020-0090-8
34. Wang S, Zhang X, Liu Y, et al. Osteopontin targeted non-invasive nanoprobes with amplified surface plasmon resonance for photothermally enhanced multimodal precision imaging of vulnerable atherosclerotic plaques. *Chem Eng J*. 2023;471. doi:10.1016/j.cej.2023.144400
35. Zhu W, Dong Y, Xu P, et al. A composite hydrogel containing resveratrol-laden nanoparticles and platelet-derived extracellular vesicles promotes wound healing in diabetic mice. *Acta Biomater*. 2022;154:212–230. doi:10.1016/j.actbio.2022.10.038
36. Yang SY, Hu Y, Zhao R, et al. Quercetin-loaded mesoporous nano-delivery system remodels osteoimmune microenvironment to regenerate alveolar bone in periodontitis via the miR-21a-5p/PDCD4/NF-κB pathway. *J Nanobiotechnol*. 2024;22(1):94. doi:10.1186/s12951-024-02352-4
37. Guo X, Li H, Li Z, et al. Multi-stimuli-responsive pectin-coated dendritic mesoporous silica nanoparticles with Eugenol as a sustained release nanocarrier for the control of tomato bacterial wilt. *J Nanobiotechnol*. 2025;23(1):191. doi:10.1186/s12951-025-03239-8
38. Sha'at M, Ignat M, Sacarescu L, et al. Multifractal analysis and experimental evaluation of MCM-48 mesoporous silica as a drug delivery system for metformin hydrochloride. *Biomedicines*. 2024;12(12):2838. doi:10.3390/biomedicines12122838

39. Turkson V, Haller A, Jaeschke A, Hui DY. ApoE receptor-2 R952Q variant in macrophages elevates soluble LRP1 to potentiate hyperlipidemia and accelerate atherosclerosis in mice. *Arteriosclerosis Thrombosis Vasc Biol*. 2025;45(1):37–48. doi:10.1161/ATVBAHA.124.321748
40. Zhang BC, Zhang CW, Wang C, Pan DF, Xu TD, Li DY. Luteolin attenuates foam cell formation and apoptosis in Ox-LDL-stimulated macrophages by enhancing autophagy. *Cell Physiol Biochem*. 2016;39(5):2065–2076. doi:10.1159/000447902
41. Dai N, Hu Y, Tang X, et al. Cholesterol, atherosclerotic, and inflammatory risks among patients with statin therapy. *JACC Cardiovasc Imaging*. 2025;18(2):242–244. doi:10.1016/j.jcmg.2024.08.009
42. Xing Y, Lin X. Challenges and advances in the management of inflammation in atherosclerosis. *J Adv Res*. 2025;71:317–335. doi:10.1016/j.jare.2024.06.016
43. Soehnlein O, Lutgens E, Döring Y. Distinct inflammatory pathways shape atherosclerosis in different vascular beds. *Eur Heart J*. 2025;46:3261–3272. doi:10.1093/eurheartj/ehaf054
44. Monaco C, McNamara CA, Slütter B, et al. Immunotherapy for atherosclerosis. *Physiol Rev*. 2025. doi:10.1152/physrev.00016.2024
45. Wang ZC, Niu KM, Wu YJ, et al. A dual Keap1 and p47(phox) inhibitor Ginsenoside Rb1 ameliorates high glucose/ox-LDL-induced endothelial cell injury and atherosclerosis. *Cell Death Dis*. 2022;13(9):824. doi:10.1038/s41419-022-05274-x
46. Li Y, Zhou M, Li H, et al. Macrophage P2Y6 receptor deletion attenuates atherosclerosis by limiting foam cell formation through phospholipase Cβ/store-operated calcium entry/calreticulin/scavenger receptor A pathways. *Eur Heart J*. 2024;45(4):268–283. doi:10.1093/eurheartj/ehad796
47. Wang H, Guo J, Xiu T, et al. H(2)O(2) accumulation promoting internalization of ox-LDL in early atherosclerosis revealed via a synergistic dual-functional NIR fluorescence probe. *Chem Sci*. 2024;16(1):345–353. doi:10.1039/D4SC05546B
48. Huang HC, Wang TY, Rousseau J, et al. Biomimetic nanodrug targets inflammation and suppresses YAP/TAZ to ameliorate atherosclerosis. *Biomaterials*. 2024;306:122505. doi:10.1016/j.biomaterials.2024.122505
49. Wang L, Zhang X, Zhang H, et al. Novel metal-free nanozyme for targeted imaging and inhibition of atherosclerosis via macrophage autophagy activation to prevent vulnerable plaque formation and rupture. *ACS Appl Mater Interfaces*. 2024;16(39):51944–51956. doi:10.1021/acsami.4c08671
50. Zhang J, Wang Z, Liao Y, et al. Black phosphorus nanoplatform coated with platelet membrane improves inhibition of atherosclerosis progression through macrophage targeting and efferocytosis. *Acta Biomater*. 2025;192:377–393. doi:10.1016/j.actbio.2024.11.041
51. Jin Y, Lu J, Liu F, Yang X, Chen F, Zhang J. MiR-4291 stabilized the vulnerable atherosclerotic plaques by degrading the MAPK1/ERK2 in ApoE (-/-) mice. *Ann Translat Med*. 2022;10(22):1243. doi:10.21037/atm-22-5241
52. Wang Y, Wang J, Zheng W, et al. Identification of an IL-1 receptor mutation driving autoinflammation directs IL-1-targeted drug design. *Immunity*. 2023;56(7):1485–1501.e1487. doi:10.1016/j.immuni.2023.05.014
53. Warnatsch A, Ioannou M, Wang Q, Papayannopoulos V. Inflammation. Neutrophil extracellular traps license macrophages for cytokine production in atherosclerosis. *Science*. 2015;349(6245):316–320. doi:10.1126/science.aaa8064
54. Corbera-Bellalta M, Kamberovic F, Alba-Rovira R, et al. The IL-6 axis in vascular inflammation: effects of IL-6 receptor blockade on vascular lesions from patients with giant-cell arteritis. *Ann Rheumatic Dis*. 2025;84:1387–1400. doi:10.1016/j.ard.2025.02.008
55. Cominacini L, Garbin U, Mozzini C, et al. The atherosclerotic plaque vulnerability: focus on the oxidative and endoplasmic reticulum stress in orchestrating the macrophage apoptosis in the formation of the necrotic core. *Curr Med Chem*. 2015;22(13):1565–1572. doi:10.2174/092986732266150311150829
56. Dai MX, Zheng XH, Yu J, et al. The impact of intermittent and repetitive cold stress exposure on endoplasmic reticulum stress and instability of atherosclerotic plaques. *Cell Physiol Biochem*. 2014;34(2):393–404. doi:10.1159/000363008
57. Ren JL, Chen Y, Zhang LS, et al. Intermedin(1-53) attenuates atherosclerotic plaque vulnerability by inhibiting CHOP-mediated apoptosis and inflammasome in macrophages. *Cell Death Dis*. 2021;12(5):436. doi:10.1038/s41419-021-03712-w
58. Wang X, Huang J, Hou H, Chen D. The relationship with the stability between GRP78, CHOP and human carotid atherosclerotic plaque. *Clin Neurol Neurosurg*. 2022;212:107067. doi:10.1016/j.clineuro.2021.107067
59. Wei HJ, Xu JH, Li MH, et al. Hydrogen sulfide inhibits homocysteine-induced endoplasmic reticulum stress and neuronal apoptosis in rat hippocampus via upregulation of the BDNF-TrkB pathway. *Acta Pharmacol Sin*. 2014;35(6):707–715. doi:10.1038/aps.2013.197